ACS APPLIED MATERIALS & INTERFACES

Research Article

www.acsami.org

Toward Single-Mode Active Crystal Fibers for Next-Generation High-Power Fiber Devices

Chien-Chih Lai,*[,†] Wan-Ting Gao,[†] Duc Huy Nguyen,[†] Yuan-Ron Ma,[†] Nai-Chia Cheng,[‡] Shih-Chang Wang,[‡] Jeng-Wei Tjiu,[§] and Chun-Ming Huang[∥]

[†]Department of Physics, National Dong Hwa University, Hualien 97401, Taiwan

[‡]Institute of Photonics and Optoelectronics, National Taiwan University, Taipei 10617, Taiwan

[§]Department of Dermatology, National Taiwan University Hospital and College of Medicine, National Taiwan University, Taipei 10002, Taiwan

[∥]Department of Material Science and Engineering, National Cheng Kung University, Tainan 70101, Taiwan

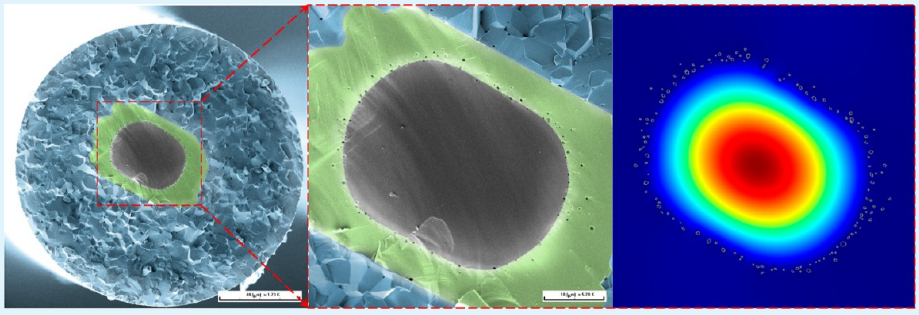

ABSTRACT: We report what we believe to be the first demonstration of a facile approach with controlled geometry for the production of crystal-core ceramic-clad hybrid fibers for scaling fiber devices to high average powers. The process consists of dip coating a solution of polycrystalline alumina onto a high-crystallinity 40-μm-diameter Ti:sapphire single-crystalline core followed by thermal treatments. Comparison of the measured refractive index with high-resolution transmission electron microscopy reveals that a Ca/Si-rich intragranular layer is precipitated at grain boundaries by impurity segregation and liquid-phase formation due to the relief of misfit strain energy in the Al_2O_3 matrix, slightly perturbing the refractive index and hence the optical properties. Additionally, electron backscatter diffractions supply further evidence that the Ti:sapphire single-crystalline core provides the template for growth into a sacrificial polycrystalline cladding, bringing the core and cladding into a direct bond. The thus-prepared doped crystal core with the undoped crystal cladding was achieved through the abnormal grain-growth process. The presented results provide a general guideline both for controlling crystal growth and for the performance of hybrid materials and provides insights into how one might design single-mode high-power crystal fiber devices.

KEYWORDS: *fiber, fiber laser, high power, sapphire, ceramics*

1. INTRODUCTION

In the field of high-power active single-mode fiber devices, the exploration of materials with unique properties as relevant alternatives to existing glass-based fibers is critical to achieving further improvement in the power that such devices can carry. Crystal fiber, a typical example of the crystalline-core configuration, features exceptional optical properties in comparison to conventional glass or polymer fiber,[1−4] such as a high emission cross-section and low-threshold lasing,[5−7] high thermal loading and a high laser damage threshold,[8−10] and efficient $\chi^{(3)}$ processes;[11−13] crystal fiber is expected to provide a key architecture for scaling the fiber laser power in the near future. Scaling fiber lasers and amplifiers to high average powers requires materials with high thermal conductivity such that heat can be easily dissipated from the interior, in this case, from the crystalline core of the fiber. A great variety of approaches are available nowadays to fabricate such a crystalline waveguide structure, including the modification of the spatial distribution of the refractive index (RI) difference (Δn) within the glass and crystal matrixes by femtosecond-laser inscription[14−16] or direct crystal fiber growth by a laser-based fiber-drawing system.[5−7,11] Although the former has been experimentally demonstrated to be effective for single-mode operation, the applied high-peak power often leads to a deteriorated structure, and, consequently, to a larger propagation loss, with typical values from 1 to a few dB/cm.[15] Moreover, the employed femtosecond laser source is expensive and extremely sophisticated, making its use for practical applications difficult.

These hindrances can be circumvented by the latter approach, known as the so-called laser-heated pedestal growth

Received: May 27, 2014
Accepted: July 31, 2014
Published: July 31, 2014

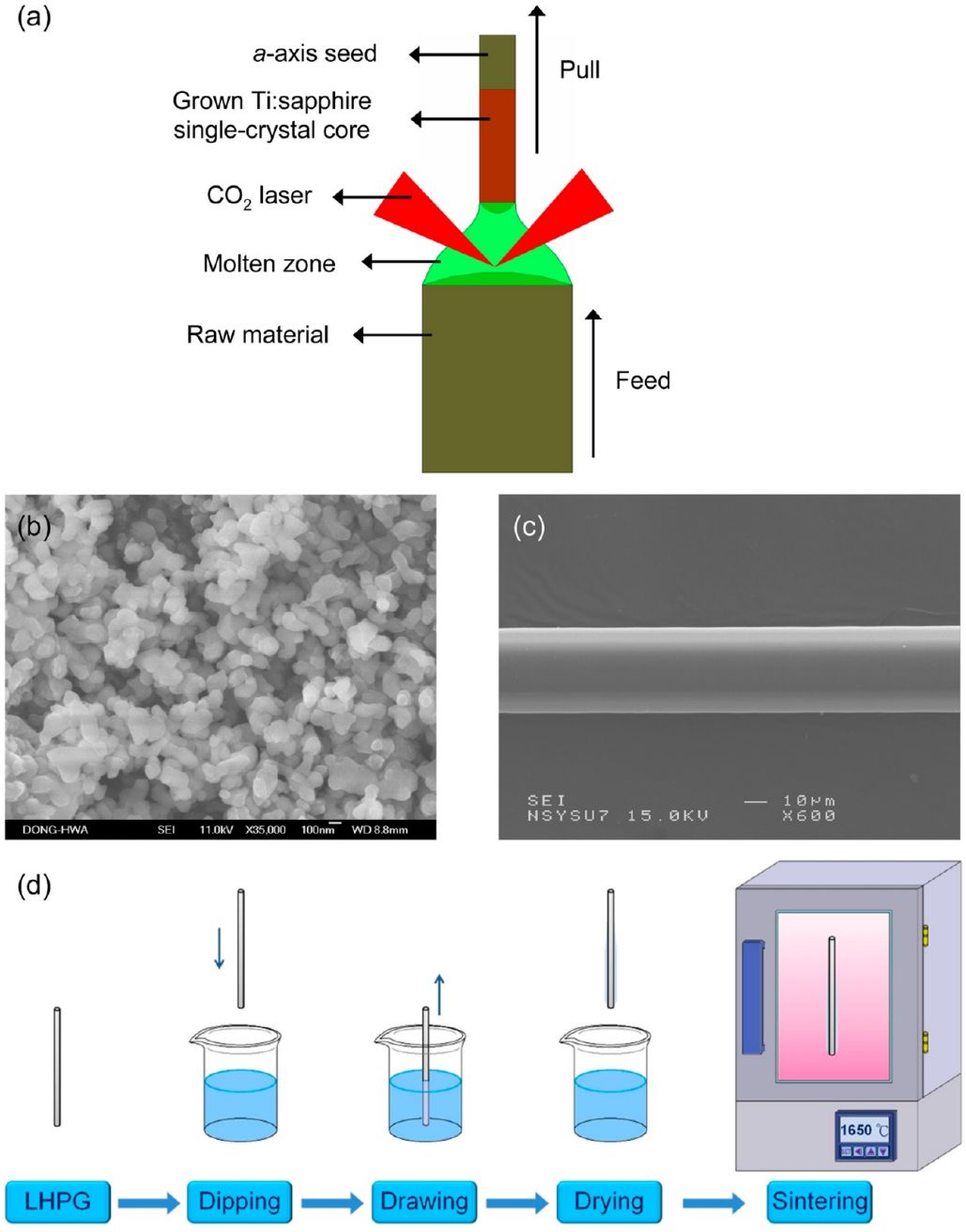

Figure 1. (a) Schematic of LHPG-grown Ti:sapphire single-crystal core. SEM observations of (a) the starting alumina power and (b) the LHPG-grown high-crystallinity 40-μm-diameter Ti:sapphire single-crystal core. (c) Schematic of crystal−ceramic hybrid fiber fabrications.

(LHPG) technique. This technique is a simple yet effective method for creating a high-crystallinity core with a low propagation loss (<0.1 dB/cm) and a strong index guiding, which is caused by the large Δn between the crystal core and glass cladding.[11,17−19] This large Δn, however, usually accompanies a large number of propagation modes and is considered problematic for most applications. Because the presence of a multimode output is a crucial concern for the LHPG-grown crystal fiber, it is important to introduce a cladding that has a RI slightly less than that of the fiber core. For example, this problem could be ameliorated by using a cladding with high-index glass to reduce the number of guided modes, which, however, results in degradation of few-mode operation in a restricted bandwidth.[20] This is because the dispersion curves of the crystal core and the high-index glass cladding intersect only for a few individual wavelengths. Although fabricating a high-index glass cladding for the LHPG-grown crystal fiber is straightforward, achieving nearly single-mode operation over a wide spectral range remains challenging, especially in the long-wavelength regions. Furthermore, a glass cladding introduces a major bottleneck for pursuing significant power scaling with high heat dissipation between the crystalline core and the heat sink.

A doped crystal core with undoped crystal cladding can offer a straightforward approach to a truly single-mode operation over a broad bandwidth in a structure that allows a high heat load. This concept has proven feasible in efficient crystalline waveguide lasers but is costly to produce.[21] As promising alternatives for single-mode realization in a cost-effective way, bulk ceramics have been shown to be exceptionally successful in

laser gain media that exhibit extremely low scattering loss and high fracture-limited laser intensity, equivalent to those obtained in bulk crystals.[22−24] In contrast, a ceramic fiber without a cladding shows a rather large scattering loss due to the presence of grain boundaries and pores that reduce optical quality. The surface roughness of the ceramic fiber, however, is often poor and further exacerbated by the large Δn at the fiber/air interface as can been seen by examining the light passing down the unclad fiber.[25] Ultimately, a desirable configuration, consisting of a doped crystalline core with an undoped polycrystalline (ceramic) cladding, has emerged because of its potential to overcome the aforementioned limits by combining the respective advantages of crystalline and ceramic materials: that is, a relatively low Δn and a high thermal conductivity respectively assist with the objectives of single-mode operation and high-power operation. However, to our knowledge, this crystal-core ceramic-clad hybrid waveguide structure has not been reported. A better understanding of its potential makes it clear that there is an urgent need for further optical and structural investigations.

Here, we present a controlled process for the production of a Ti:sapphire-crystal-core/alumina-ceramic-cladding hybrid fiber through dip coating with a solution of polycrystalline alumina. The results from fabricating and studying this crystal−ceramic hybrid fiber may serve as a guide to the future fabrication of single-mode high-power crystal fiber devices.

2. EXPERIMENTAL SECTION

2.1. Crystal−Ceramic Hybrid Fiber Fabrications. Figure 1 shows the detailed procedures by which Ti:sapphire-crystal-core/alumina-ceramic-ladding hybrid fibers are prepared. In the first step, an *a*-axis sapphire square rod (0.5 mm × 0.5 mm in cross-section) grown by the Czochralski method was used as the row material. As shown in Figure 1a, the raw material is heated by a 100-W 10.6-μm CO_2 laser to melt the top end, and then the seed rod is dipped into the molten zone. A single-crystalline fiber is grown by pulling the seed rod and feeding the raw material upward simultaneously at a constant growth ratio. Through three diameter-reduction steps by the LHPG technique, a 40-μm-diameter Ti:sapphire single-crystal core was grown in an ambient, followed by dip coating in aqueous-based alumina suspensions. The variation of the core diameters was within 5%. The length of the grown fiber can be as long as 50 cm, depending on the fiber drawing system. The high purity of 99.99% α-alumina AKP-50 (Sumitomo Chemical Co.),[26] having an average powder size of 0.2 μm, was used as the starting material under the cladding, as imaged by a scanning electron microscope (SEM, JSM-6500F, JEOL), where the resulting image is shown in Figure 1b. Figure 1c shows the SEM (JXA-8900R, JEOL) side view of a LHPG-grown 40-μm-diameter Ti:sapphire crystal core with uniform diameter and smooth surface along the fiber. Chemical analyses of the starting powder were performed by an inductively coupled plasma mass spectrometer (ICP-MS, 7500ce, Agilent). The chemical compositions of the as-received AKP-50 alumina are listed in Table 1. The total impurities did not exceed 100 ppm. Figure 1d shows the schematic diagram of the fabrication of a Ti:sapphire-crystal-core/alumina-ceramic-cladding hybrid fiber by the dip-coating technique. The submicrometer-sized alumina powders were ball-milled in an alumina bottle to perfectly disperse it. After that, the alumina powder was mixed with the additives in ethyl alcohol and dip-coated onto the surface of the LHPG-grown 40-μm-diameter Ti:sapphire core. Finally, the as-prepared crystal−ceramic hybrid fibers were sintered in air for 2 h at 1650 °C in a high-purity alumina tube furnace (Lenton, LTF 18/75/300). Note that the dip-coating process was conducted at room temperature. Temperature-induced cladding enables coagulation of aqueous suspensions at elevated temperatures due to higher chemical reaction rates. It was found that elevated temperatures lead to faster coagulation during hydrolysis, which, in turn, results in unintentionally introduced periodic undulations in the ceramic cladding. On the other hand, both the dipping speed and the incident angle of the fiber primarily influence the meniscus shape at the solid/liquid interface and hence the thickness of the ceramic coating. Greater speeds and larger angles give thicker cladding. However, an increase in angle results in a significant increase in the amount of pores due to the presence of an unbalanced liquid surface tension around the fiber. The key consideration in achieving cladding of uniform coating on the fiber is the strain between the fiber and aqueous suspensions. The liquid contact angle at the periphery of the fiber should be kept constant (i.e., perpendicularly dipping) so that the interfacial adhesion properties are controlled and pore-free ceramic cladding is achieved.

Table 1. Chemical Analyses of Starting Alumina (AKP-50)

composition	AKP-50 (ppm) (measured in this work)	AKP-50 (ppm) (provided by Sumitomo)
Ca	40 ± 10	
Si	50 ± 10	≤25
Mg	<5	≤10
Fe		≤20
Cu		≤10

2.2. Nanostructural and Optical Characterizations. Electron backscatter diffraction (EBSD, JSM-7001F, JEOL) was employed to determine the crystallographic orientations of the crystal core and ceramic cladding. The nanostructure of the crystalline-core/intercrystalline-inner-clad interface was investigated with a field-emission high-resolution transmission electron microscope (HR-TEM, Tecnai G^2 F20, FEI) operating at 200 kV. Energy dispersive X-ray (EDX) analyses were performed in an HR-TEM. To study the migrated boundary (i.e., the crystal-core/ceramic-clad interface) just below the surface, a dual-beam focused ion beam (FIB, SMI3050, Seiko) combined with a standard FIB lift-out technique was used to prepare the cross-sectional HR-TEM specimen.[27] A benefit of using site-specific specimen preparation by FIB is that it allows for the migration of the boundary to accurately be determined. The corresponding RI profiles of the finely polished fiber faces were measured by using a depolarized 633 nm laser scanning confocal microscope (TCS SP2, Leica). The refractive index profile of the fiber was measured according to the normal incident Fresnel reflection. This method relies on the Fresnel relation between the refractive index n of the material and its reflectivity R. The relation can be expressed as $R = [(n - 1)/(n + 1)]^2$.

3. RESULTS AND DISCUSSION

3.1. Morphology Investigations and Intercrystalline-Layer Growth Mechanism. Figure 2a−c shows the representative side and end views of the fracture morphology of an as-sintered crystal−ceramic hybrid fiber revealing its granular structure. Note that several of the grains that were grown appear columnar in cross-section, as demonstrated in the side view of the fiber (as marked by the arrows in Figure 2b). The alumina shows an elongated morphology, with the basal plane parallel to the long axis of the grains. The development of elongated grains, known as abnormal grain growth (AGG), is often associated with the presence of substantial amounts of liquid phase and impurity segregation, as are discussed in detail later. Figure 2d shows the statistical distribution of the grain sizes in the hybrid fiber. It is obvious that most grains have a diameter of about 4−8 μm, with the average size being approximately ~6.54 μm. The varying diameter can be extracted by a log-normal distribution function as follows:[28]

$$f_N(w) = \frac{A}{w\sigma\sqrt{2}} \exp\left[-\frac{\ln(w/\bar{w})}{2\sigma^2}\right] \quad (1)$$

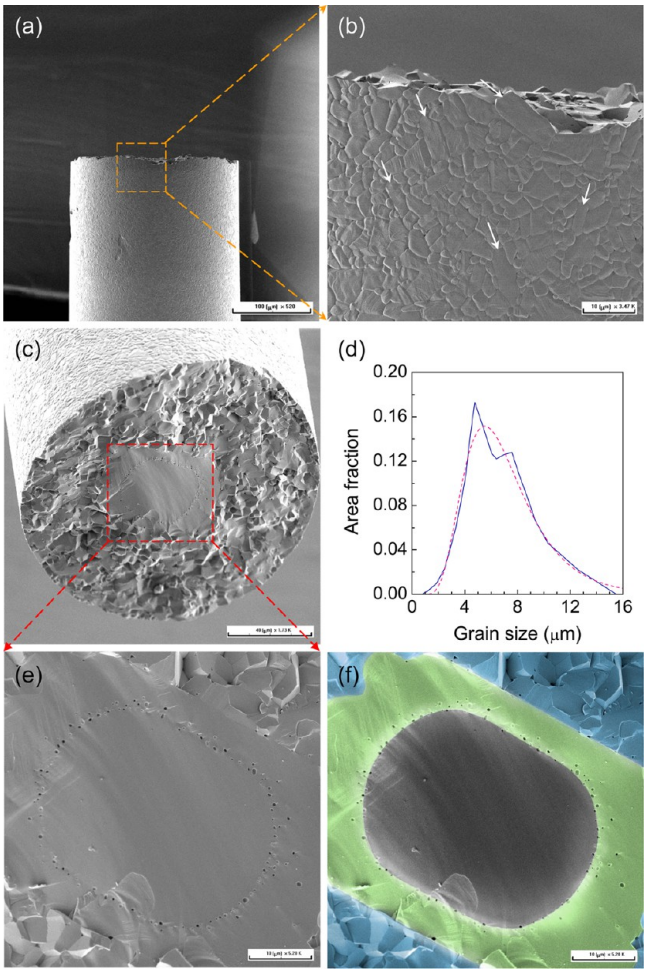

Figure 2. Fracture morphology of a crystal−ceramic hybrid fiber revealing its granular structure. (a,b) Side views, showing the presence of the faceted and abnormal lath-like grain growth (as marked by the arrows). (c,e) End view along the *a* axis. (d) Grain size distribution, fitted by a log-normal distribution function. The average grain size is around ∼6.54 μm. (f) Schematic of the hybrid fiber structure of the fiber from the perspective shown in (e), indicating that the crystalline-core seed grew into the alumina polycrystalline cladding, resulting in an intercrystalline layer (i.e., inner cladding).

where w is the size of the grain; $\bar{w}$ (=6.54 ± 0.15 μm) is the average size of the grains; A (=0.94 ± 0.32) is the initial constant; and σ (=0.41 ± 0.02) is the standard deviation of the sizes of the grains. The slightly larger standard deviation of the size distribution ($\sigma \geq 0.25$) is also an indication of the presence of the anisotropic faceted AGGs, as shown in Figure 2b. Moreover, the grain growth rate K in the as-annealed sample obeys the kinetic law. This law can be expressed as[29]

$$G^3 - G_0^3 = Kt \quad (2)$$

where G and G_0 are the average grain size at times t and $t = 0$, respectively. The experimentally determined values for G, G_0, and t are 6.54 μm, 0.20 μm, and 7200 s, respectively. The calculated K of this case is $\sim 4 \times 10^{-20}$ m^3/s, which compares favorably with the reported case containing liquid phase at 1600 °C (3×10^{-20} m^3/s) and 1500 °C (5×10^{-20} m^3/s), respectively.[29,30]

Figure 2e shows a magnified version of the image of the *a*-axis Ti:sapphire core in Figure 2c. The orientation of the Ti:sapphire crystalline core can be easily determined through the 2-fold nature, which is the typical character of *a*-axis sapphire.[31] From Figure 2c and e, the most striking feature of the fracture morphology is the faceting observed as the Ti:sapphire crystalline-core seed grew into the alumina polycrystalline cladding, as depicted in the corresponding schematic in Figure 2f. In Figure 2f, the dark gray color represents the pristine Ti:sapphire core seed, while the green and blue represent the intercrystalline inner cladding and the ceramic outer cladding. It is also noteworthy that the intercrystalline layer exhibits basal facets with the nearly planar growth front; in contrast, the growth of the prismatic-plane crystal core seed into the polycrystalline cladding is highly nonuniform. Of particular interest in Figure 2c and e is the fact that the growth rates are also functions of the crystallographic orientation, as predicted by the molecular dynamics simulations.[32] The growth rate perpendicular to the basal facets is much lower than that of all other crystallographic directions. The difference in growth rate is caused by the occurrence of the liquid phase. As the sintering is performed with a certain amount of liquid phase, the basal liquid−solid interfaces are relatively immobile, while nonbasal facets wetted by the liquid phase are able to move more freely. A significant amount of liquid-phase films has been observed by HR-TEM in commercial alumina powders that contain ∼0.2% impurities.[33,34] We note that alumina has a very limited solubility for most of the impurities.[35] In those samples, strong segregation of impurities, which confines them to the grain boundaries, occurs to reduce the impurity concentration within the grains to below the solubility limit. During the sintering and grain growth, the grain boundary area is reduced, and the solute in the grain boundary area increases. As a result, the capacity of the grain boundary will be exceeded at a critical grain size, and, hence, a liquid phase will appear. Previously, there have been publications that postulated that most sintered alumina samples were unintentionally introduced under typical laboratory processing by the ubiquitous CaO and SiO_2 impurities.[36,37] The segregations of Ca and Si presumably are due to the low solubility and the relief of misfit strain energy in an Al_2O_3 matrix. For example, Ca^{2+} is roughly twice the size of Al^{3+} based on their Pauling radii. These impurities will be segregated to the grain boundary or will be present as a liquid phase due to the low solubility and large ionic radii of Ca and Si in an Al_2O_3 matrix. The presence of small amounts of CaO or SiO_2 has a strong tendency to stimulate AGG during the sintering of alumina;[38−40] moreover, the threshold concentration for AGG was lower when they coexisted. On the other hand, grain morphology becomes more equiaxed as the impurity level is reduced[30,41−43] or by introducing a small amount of MgO.[38−42,44−50] This implies that AGG during sintering is associated with the existence of a liquid phase. The aforementioned results also indicate that excess Ca and Si impurities have been shown to play an important role in faceting and promote abnormal lath-like grain growth, as shown in Figure 2b. This correlation is similar to those found in relatively pure polycrystalline Ni and Ag.[51,52] In our case, as can be seen in Table 1, our starting materials contain detectable concentrations of Ca and Si, producing AGG, faceted grain, and liquid phase, as observed in other $CaO-Al_2O_3-SiO_2$ systems.[29,30,41,53,54]

We now discuss how anisotropic growth rates caused by the Ca and Si inclusions can facilitate intercrystalline layer growth. Figure 3a shows a typical inverse pole figure (IPF) plot of the crystal−ceramic hybrid fiber, which demonstrates that a high

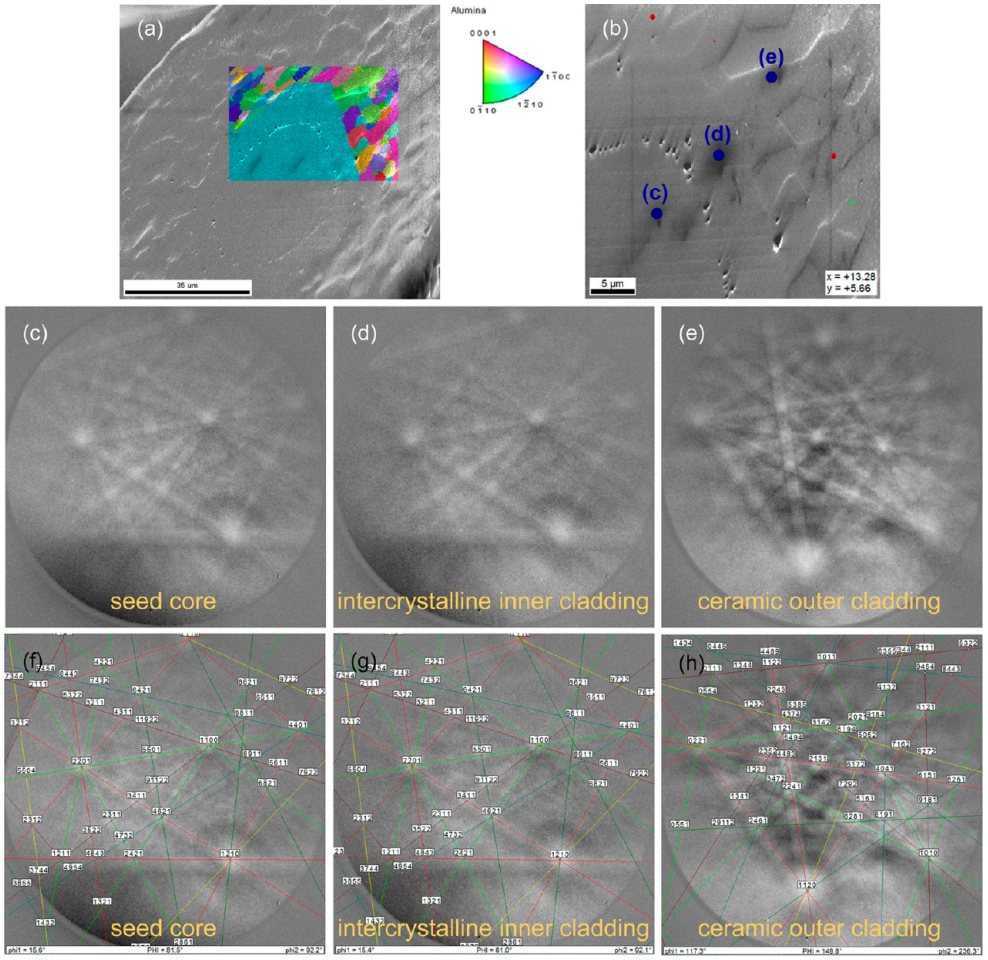

Figure 3. EBSD analyses of the cross-section of the crystal−ceramic hybrid fiber. (a) An inverse pole figure (IPF) map is superimposed on an SEM micrograph of the fiber cross-section, yielding the correspondence between the crystallographic direction and the core, inner cladding, and outer cladding, respectively. The color of the grains indicates the crystallographic direction parallel to the fiber axis. (b) The Kikuchi patterns acquired in different positions. (c−e) The corresponding Kikuchi patterns without the indexing overlay. (f−h) The corresponding Kikuchi patterns with the indexing overlay.

crystallinity of AGG exists along the *a*-axis core seed. The AGG mechanism has been shown to be a key factor in converting polycrystalline alumina into a large single-crystal sapphire.[55] The color-coded IPF was acquired with a tilted sample to give contrast to the intercrystalline inner cladding and in preparation for the EBSD collection. Figure 3b−d shows the corresponding indexed Kikuchi patterns of the crystal seed core, intercrystalline inner cladding, and ceramic outer cladding (i.e., faceted grains), respectively. It was determined that these three regions have the corundum structure of α-Al_2O_3. From the EBSD results depicted in Figure 3, the orientation of this intercrystalline inner cladding can also be precisely determined through the direction of the Ti:sapphire crystal core, which shows the same crystallographic direction and a similarly elongated morphology with the basal plane parallel to the long axis of the core. The indexing of the EBSD patterns demonstrates that the intercrystalline inner cladding has the same crystallographic orientation as the seed core. Additionally, we observed uniformly separated pores left behind by the intercrystalline migrating interface marking the origin of the crystal-core/ceramic-clad interface after 2 h at 1650 °C. By assuming the interface migration time to be 7200 s (i.e., 2 h of annealing time), values of the average growth rate V of the intercrystalline inner cladding into the polycrystalline outer cladding of about 6.25×10^{-4} and 15.28×10^{-4} μm/s can be obtained for thickness values of this layer along the basal and nonbasal plane of ∼4.5 and ∼11.0 μm, respectively. The corresponding interface mobilities M for the seed crystal core in both the basal and the nonbasal planes can be estimated using[41]

$$M = \frac{VG}{3\gamma} \tag{3}$$

where γ is the isotropic grain-boundary energy and G is the average cladding grain size. Considering all of the data for V, γ, and G of 6.25×10^{-4} μm/s (basal planes), 15.28×10^{-4} μm/s (nonbasal planes), 0.3 J/m^2, and 6.54 μm, the resulting M values for the seed core were determined to be $\sim 4.54 \times 10^{-15}$ (basal planes) and 11.1×10^{-15} m^3 N^{-1} s^{-1} (nonbasal planes), respectively. These results are in satisfactory agreement with the experimentally determined values of $\sim 1.00 \times 10^{-15}$ and 3.00×10^{-15} m^3 N^{-1} s^{-1} for the basal and nonbasal planes.[29,41]

Growth of single-crystal sapphire into polycrystalline alumina was first observed in 1974.[56] Recently, this conversion process has been widely applied to commercial high-pressure sodium lamps.[57] An intercrystalline inner cladding forms as a small fraction of the grains grow to abnormally large size by consuming adjoining smaller grains. The exaggerated grain growth is driven by the reduction in surface free energy because

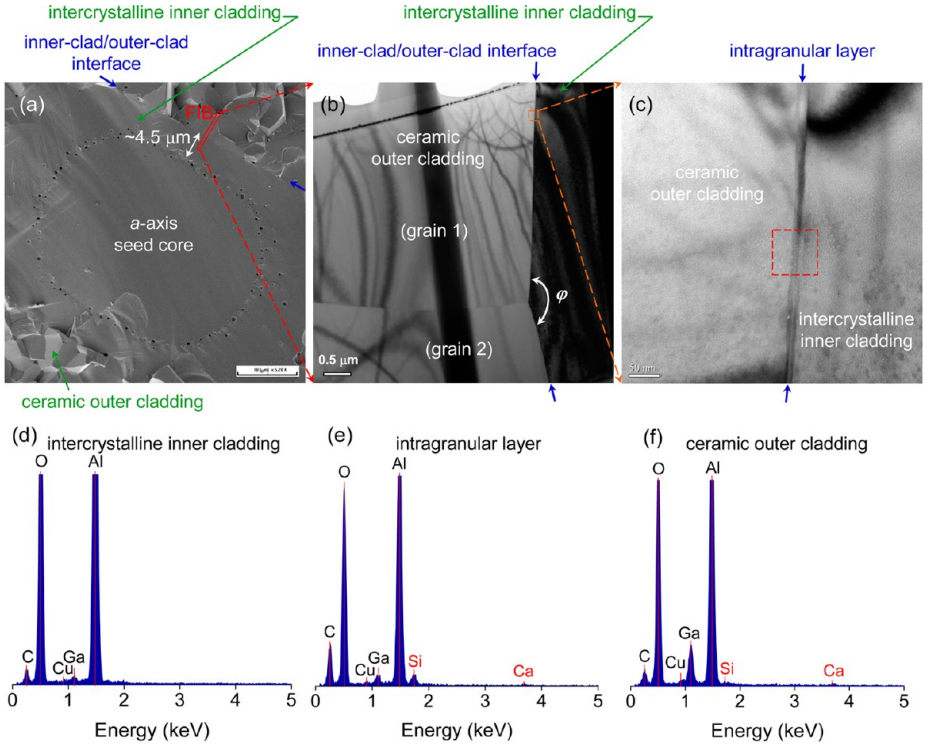

Figure 4. (a) SEM scan of a region of an inner-clad/outer-clad interface where the original boundary has migrated ~4.5 μm. The analyzed FIB location prepared as the TEM specimen is marked in the figure. (b) Low-magnification TEM image of an FIB section taken at a boundary (i.e., inner-clad/outer-clad interface) that has migrated within the hybrid fiber. (c) High-magnification TEM image of an enlargement in (b), showing an intragranular layer in between intercrystalline inner cladding and ceramic outer cladding. Representative EDX spectra of the inner cladding, outer cladding, and intragranular layer are shown in (d)−(f), respectively. The presence of both Ca and Si signals in (e) indicates that a Ca/Si-rich intragranular layer is precipitated at grain boundaries by impurity segregation and liquid-phase formation.

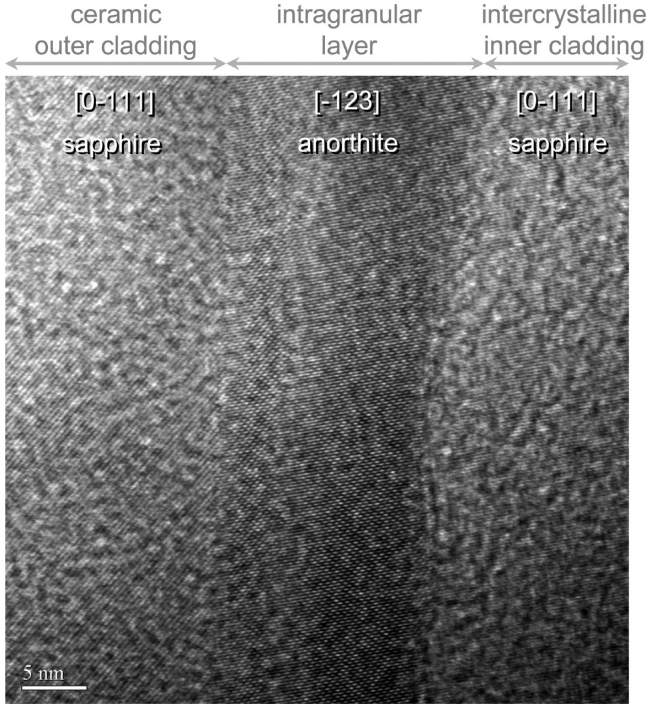

Figure 5. HR-TEM image of the inner-clad/outer-clad interface, showing the intragranular layer (crystalline anorthite) between the inner and outer cladding.

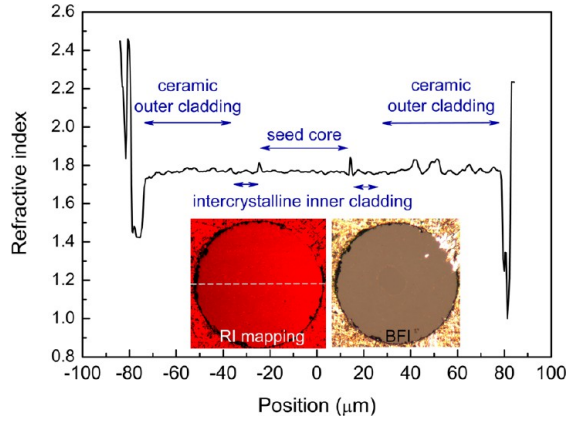

Figure 6. RI profile of the crystal−ceramic hybrid fiber. The insets show the corresponding RI mapping and BFI of the hybrid fiber, respectively.

a single large grain has a lower surface area as compared to a large number of smaller grains. This process brought the single-crystal Ti:sapphire core and intercrystalline inner cladding into a direct bond, forming a doped crystal core with an undoped crystal cladding structure. Ultimately, a doped crystal core with an undoped crystal cladding can offer a truly single-mode architecture under high-power operation.

3.2. Correlations between Ionic Segregation and Crystalline Precipitation. So far, experimental evidence relating the grain boundary nanostructure in alumina and segregation in ionic oxide to their polycrystalline-to-crystal behavior is very scarce, especially in the fiber format. In this section, we show direct observation of how Ca and Si trigger the formation of an intragranular layer between the crystal seed

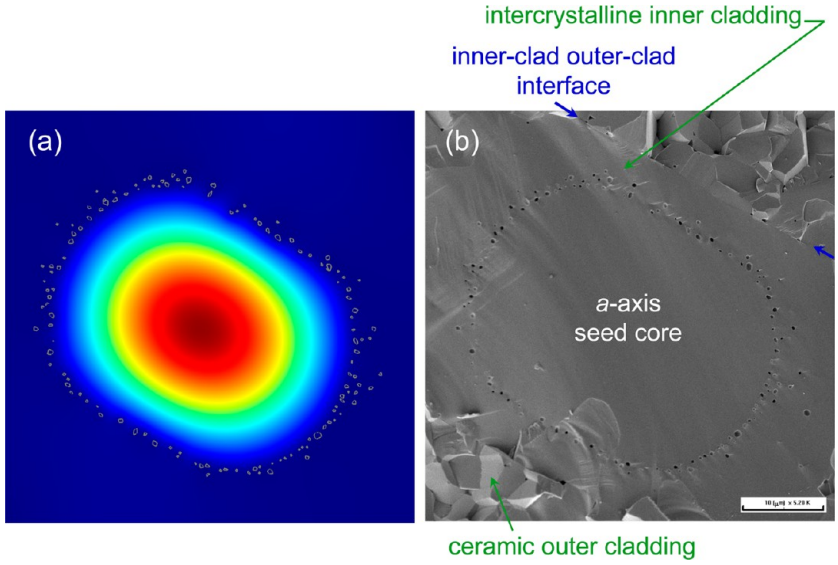

Figure 7. (a) Calculated 800 nm mode-field pattern, obtained on the basis of the RI profile in Figure 6, together with the cross-section SEM image in (b) for comparison. The result shows the effectiveness of reducing the guiding modes on the waveguide properties.

core and the sacrificial polycrystalline cladding through AGG, and thus cause them to form a tight bond. Figure 4a shows an SEM scan of the as-sintered crystal-core ceramic-clad hybrid fiber. Figure 4b shows a low-magnification TEM image, corresponding to the FIB location marked in Figure 4a. From Figure 4b, it is noticeable that the intercrystalline layer boundaries meet two discontinuously growing grains (labeled as "grain 1" and "grain 2") at an apparent dihedral angle (φ) of nearly 180°. As suggested by the interpretations of previous works,[30,58] this unambiguous structure demonstrates the presence of a continuous liquid film along the intercrystalline-inner-clad/polycrystalline-outer-clad interface at the sintering temperature. In comparison with the EDX results, at the present stage of the inclusion of CaO and SiO_2, the stable phase is a liquid-phase calcium aluminosilicate. These phases produce distinctly different EDX signatures, as illustrated in Figure 4d–f. Representative EDX spectra in Figure 4d–f exhibit the main Al and O peaks, while the Cu and Ga signals originate from the supporting copper grid and the FIB ion gun, respectively. The EDX spectrum in Figure 3e features an Al-, Si-, and Ca-containing intragranular phase.

Given the fact that the case we are considering is at the Al_2O_3-rich end of the ternary phase diagram,[59] the possible second-phase precipitate in the equilibrium was anorthite ($CaAl_2Si_2O_8$). Note that an anorthite and alumina matrix mixture has a liquid phase at 1380 °C. Thus, it was expected that there would be a crystalline anorthite grain boundary layer in our samples sintered at 1650 °C, as is evident in Figure 5. Figure 5 shows the magnified image of the area bounded by the dashed red square in Figure 4c. HR-TEM observations reveal that all fiber samples that include anorthite precipitate exhibited a crystalline layer over the majority of the intercrystalline-inner-clad/polycrystalline-outer-clad interface. The intragranular layer thickness measured from Figure 5 was typically 10–15 nm. The precise thickness for a specific sample was observed to vary from boundary to boundary.

3.3. Optical Analyses of the Crystal–Ceramic Hybrid Fiber. Having demonstrated that the Ti-doped sapphire crystalline core is bounded quite well in the surrounding undoped intercrystalline inner cladding, we now investigate the crucial optical properties regarding the RI and modal distributions. Figure 6 shows the RI profile of the crystal-core ceramic-clad hybrid fiber as a function of the position along the *X* direction, together with the RI mapping and the bright field image (BFI) for comparison. The RIs of the doped crystal core and undoped intercrystalline inner cladding are about 1.76817 and 1.76815, respectively. Fluctuations seem to appear in the polycrystalline outer cladding, resulting from some unintentional scratches. Additionally, the rounding of the profile edges is also a well-known artifact of mechanical preparation caused by the edge effect.[60] Another salient feature is that the core shows a plateau profile, but two sharp spikes begin to emerge at the core boundary, which is a signature of the crystal-core/intercrystalline-inner-clad interface, as can be seen by the naked eye from the BFI in Figure 6. This feature is most likely caused by emissive color centers,[61] in this case, the existence of Ca/Si-rich precipitates in the cladding. These sharp bright spots can be ascribed to the large emission cross sections of the color centers, and it is contributed to by the phonon-driven odd-parity vibrations.

To acquire a quantitative understanding of the guiding effect, two-dimensional finite-element-method calculations of the mode-field pattern were performed on the basis of the RI profile in Figure 6. A realistic representation of the pore cross sections at the seed-core/intercrystalline-clad interface was obtained by identifying the fiber contours in the SEM image. The modal pattern for the guided LP_{01} mode at 800 nm is superimposed on approximately scaled pores (gray circles) to show the relative position of the mode-field pattern and the orientation of the crystal core. As revealed in the optical model in Figure 7, a simple reduction in Δn shows the effectiveness of reducing the guiding modes on the waveguide properties. In addition, the contours included in Figure 7 clearly reveal that the waveguide has a mode profile with 2-fold symmetry. The $1/e^2$ intensity mode-field diameters are measured to be ~28.2 and 35.0 μm along the basal and nonbasal planes, respectively. As one can see, the mode-field diameters are slightly perturbed at the core/inner-clad interface, which could be the result of a tighter cladding confinement due to the presence of the faceted pores. The above result indicates that the crystal–ceramic

hybrid fiber acts as a single-transverse-mode output through a combination consisting predominantly of the crystal seed core, intercrystalline inner cladding, and polycrystalline outer cladding.

4. CONCLUSION

We have reported on the fabrication of a crystal-core ceramic-clad hybrid architecture in the crystalline fiber format for the first time to our knowledge. The core and cladding are based on the Ti:sapphire crystal and polycrystalline alumina. The morphology and nanostructure of the dip-coating-prepared hybrid fiber were also revealed as well. The thus-fabricated hybrid fiber consists of not only a doped crystal core and a ceramic outer cladding but also an AGG-induced intercrystalline undoped inner cladding, which remains challenging to create in crystal-based single-mode fibers. The dip-coating technique offers an efficient and more cost-effective approach to developing single-mode high-power fiber devices, when compared to conventional techniques such as femtosecond-laser inscription and the use of high-index-glass cladding. Future efforts will be devoted to reducing the number of pores formed at the core/inner-clad interface, ensuring the unperturbed guidance properties. This proof of concept opens the prospect of creating single-mode fibers from any crystalline material while attaining high crystallinity and hence a high damage threshold.

AUTHOR INFORMATION

Corresponding Author

*Tel.: +886-3-863-3738. Fax: +886-3-863-3690. E-mail: cclai@mail.ndhu.edu.tw.

Notes

The authors declare no competing financial interest.

ACKNOWLEDGMENTS

We are grateful to Prof. S. L. Huang at National Taiwan University for insightful discussions. We also thank L. C. Wang and Y. W. Chen for conducting the HR-TEM and FIB experiments at the facilities at National Sun Yat-Sen University, Kaohsiung, Taiwan. C. C. Lai acknowledges the strong funding support from the Ministry of Science and Technology (MOST) of Taiwan under the grant NSC 101-2112-M-259-005-MY3 as well as the start-up funding from the National Dong Hwa University.

REFERENCES

(1) Díez-Pascual, A. M.; Naffakh, M. Polypropylene/Glass Fiber Hierarchical Composites Incorporating Inorganic Fullerene-like Nanoparticles for Advanced Technological Applications. *ACS Appl. Mater. Interfaces* **2013**, *5*, 9691−9700.

(2) Persson, M.; Lorite, G. S.; Cho, S. W.; Tuukkanen, J.; Skrifvars, M. Melt Spinning of Poly(lactic acid) and Hydroxyapatite Composite Fibers: Influence of the Filler Content on the Fiber Properties. *ACS Appl. Mater. Interfaces* **2013**, *5*, 6864−6872.

(3) Stapleton, J. J.; Suchy, D. L.; Banerjee, J.; Mueller, K. T.; Pantano, C. G. Adsorption Reactions of Carboxylic Acid Functional Groups on Sodium Aluminoborosilicate Glass Fiber Surfaces. *ACS Appl. Mater. Interfaces* **2010**, *2*, 3303−3309.

(4) Furukawa, R. A.; Tagaya, A.; Koike, Y. Pressure Measurement Based on a Multimode Phase Retarder Plastic Optical Fiber. *ACS Appl. Mater. Interfaces* **2009**, *1*, 720−725.

(5) Lai, C. C.; Ke, C. P.; Tsai, C. N.; Lo, C. Y.; Shr, R. C.; Chen, M. H. Near-Field Lasing Dynamics of a Crystal-Glass Core−Shell Hybrid Fiber. *J. Phys. Chem. C* **2013**, *117*, 17725−17730.

(6) Lai, C. C.; Yeh, P.; Wang, S. C.; Jheng, D. Y.; Tsai, C. N.; Huang, S. L. Strain-Dependent Fluorescence Spectroscopy of Nanocrystals and Nanoclusters in Cr:YAG Crystalline-Core Fibers and Its Impact on Lasing Behavior. *J. Phys. Chem. C* **2012**, *116*, 26052−26059.

(7) Lai, C. C.; Wang, S. C.; Lin, Y. S.; Chen, T. H.; Huang, S. L. Near-Field Spectroscopy of Broadband Emissions from γ-Al_2O_3 Nanocrystals in Cr-Doped Double-Clad Fibers. *J. Phys. Chem. C* **2011**, *115*, 20289−20294.

(8) Bisson, J. F.; Feng, Y.; Shirakawa, A.; Yoneda, H.; Lu, J.; Yagi, H.; Yanagitani, T.; Ueda, K. I. Laser Damage Threshold of Ceramic YAG. *Jpn. J. Appl. Phys.* **2003**, *42*, L1025−L1027.

(9) Slack, G. A.; Oliver, D. W. Thermal Conductivity of Garnets and Phonon Scattering by Rare Earth Ions. *Phys. Rev. B* **1971**, *4*, 592−609.

(10) Foster, J. D.; Osterink, L. M. Thermal Effects in a Nd:YAG Laser. *J. Appl. Phys.* **1970**, *41*, 3656−3663.

(11) Lai, C. C.; Ke, C. P.; Liu, S. K.; Lo, C. Y.; Jheng, D. Y.; Wang, S. C.; Lin, S. R.; Yeh, P. S.; Huang, S. L. Intracavity and Resonant Raman Crystal Fiber Laser. *Appl. Phys. Lett.* **2012**, *100*, 261101.

(12) Ballato, J.; Hawkins, T.; Foy, P.; Yazgan-Kokuoz, B.; Stolen, R.; McMillen, C.; Hon, N. K.; Jalali, G.; Rice, R. Glass-Clad Single-Crystal Germanium Optical Fiber. *Opt. Express* **2009**, *17*, 8029−8035.

(13) Kim, J. H.; Chen, M. K.; Yang, C. E.; Lee, J.; Yin, S.; Ruffin, P.; Edwards, E.; Brantley, C.; Luo, C. Broadband IR Supercontinuum Generation Using Single Crystal Sapphire Fibers. *Opt. Express* **2008**, *16*, 4085−4093.

(14) Boinovich, L. B.; Domantovskiy, A. G.; Emelyanenko, A. M.; Pashinin, A. S.; Ionin, A. A.; Kudryashov, S. I.; Saltuganov, P. N. Femtosecond Laser Treatment for the Design of Electro-insulating Superhydrophobic Coatings with Enhanced Wear Resistance on Glass. *ACS Appl. Mater. Interfaces* **2014**, *6*, 2080−2085.

(15) Chen, F.; Vázquez de Aldana, J. R. Optical Waveguides in Crystalline Dielectric Materials Produced by Femtosecond-Laser Micromachining. *Laser Photonics Rev.* **2013**, *8*, 251−275.

(16) Sakellari, I.; Kabouraki, E.; Gray, D.; Purlys, V.; Fotakis, C.; Pikulin, A.; Bityurin, N.; Vamvakaki, M.; Farsari, M. Diffusion-Assisted High-Resolution Direct Femtosecond Laser Writing. *ACS Nano* **2012**, *6*, 2302−2311.

(17) Lai, C. C.; Ke, C. P.; Liu, S. K.; Jheng, D. Y.; Wang, D. J.; Chen, M. Y.; Li, Y. S.; Yeh, P. S.; Huang, S. L. Efficient and Low-Threshold Cr^{4+}:YAG Double-Clad Crystal Fiber Laser. *Opt. Lett.* **2011**, *36*, 784−786.

(18) Lai, C. C.; Tsai, H. J.; Huang, K. Y.; Hsu, K. Y.; Lin, Z. W.; Ji, K. D.; Zhuo, W. J.; Huang, S. L. Cr^{4+}:YAG Double-Clad Crystal Fiber Laser. *Opt. Lett.* **2008**, *33*, 2919−2921.

(19) Chen, J. C.; Lo, C. Y.; Huang, K. Y.; Kao, F. J.; Tu, S. Y.; Huang, S. L. Fluorescence Mapping of Oxidation States of Cr Ions in YAG Crystal Fibers. *J. Cryst. Growth* **2005**, *274*, 522−529.

(20) Hsu, K. Y.; Yang, M. H.; Jheng, D. Y.; Lai, C. C.; Huang, S. L.; Mennemann, K.; Dietrich, V. Cladding YAG Crystal Fibers with High-Index Glasses for Reducing the Number of Guided Modes. *Opt. Mater. Express* **2013**, *3*, 813−820.

(21) Ter-Gabrielyan, N.; Fromzel, V.; Mu, X.; Meissner, H.; Dubinskii, M. High Efficiency, Resonantly Diode Pumped, Double-Clad, Er:YAG-Core, Waveguide Laser. *Opt. Express* **2012**, *20*, 25554−25561.

(22) Shen, Y.; Liu, W. B.; Zong, N.; Li, J.; Bo, Y.; Feng, X. Q.; Li, F. Q.; Pan, Y. B.; Guo, Y. D.; Wang, P. Y.; Tu, W.; Peng, Q. J.; Zhang, J. Y.; Lei, W.; Cui, D. F.; Xu, Z. Y. Comparison of Laser Induced Thermal Fracture Between Polycrystalline Ceramic and Crystal Nd:YAG. *Opt. Lett.* **2014**, *39*, 1965−1967.

(23) Sangheraa, J.; Kima, W.; Villalobosa, G.; Shawa, B.; Bakera, C.; Frantza, J.; Sadowskib, B.; Aggarwalb, I. Ceramic Laser Materials: Past and Present. *Opt. Mater.* **2013**, *35*, 693−699.

(24) Ikesue, A.; Aung, Y. L. Ceramic Laser Materials. *Nat. Photonics* **2008**, *33*, 273−275.

(25) Fair, G. E.; Kim, H. J.; Lee, H. D.; Parthasarathy, T. A.; Keller, K. A.; Miller, Z. D. Development of Ceramic Fibers for High-Energy Laser Applications. *Proc. SPIE* **2011**, 8039.

(26) Sumitomo, http://www.sumitomo-chem.co.jp.

(27) Giannuzzi, L. A.; Stevie, F. A. A Review of Focused Ion Beam Milling Techniques for TEM Specimen Preparation. *Micron* **1999**, *30*, 197−204.
(28) Patil, R. A.; Devan, R. S.; Lin, J. H.; Liou, Y.; Ma, Y. R. An Efficient Methodology for Measurement of The Average Electrical Properties of Single One-Dimensional NiO Nanorods. *Sci. Rep.* **2013**, *3*, 3070.
(29) Rödel, J.; Glaeser, A. M. Anisotropy of Grain Growth in Alumina. *J. Am. Ceram. Soc.* **1990**, *73*, 3292−3301.
(30) Kaysser, W. A.; Sprissler, M.; Handwerker, C. A.; Blendell, J. E. Effect of A Liquid Phase on The Morphology of Grain Growth in Alumina. *J. Am. Ceram. Soc.* **1987**, *70*, 339−343.
(31) Dobrovinskaya, E. R., Lytvynov, L. A.; Pishchik, V. *Sapphire: Material, Manufacturing, Applications*; Springer: New York, NY, 2009; Chapter 2, pp 55−153.
(32) Zhang, S. H.; Garofalini, S. H. Molecular Dynamics Simulations of The Effect of The Composition of Calcium Alumino-Silicate Intergranular Films on Alumina Grain Growth. *J. Phys. Chem. B* **2006**, *110*, 2233−2240.
(33) Harmer, H. Use of Solid Solution Additives in Ceramic Processing. *Adv. Ceram.* **1984**, *10*, 679−696.
(34) Hansen, S. C.; Philips, D. S. Grain Boundary Microstructures in A Liquid-Phase Sintered Alumina (a-Al_2O_3). *Philos. Mag. A* **1983**, *47*, 209−234.
(35) Gülgün, M. A.; Voytovych, R.; Bischoff, E.; Cannon, R. M.; Rühle, M. Cation Segregation in an Oxide Ceramic With Low Solubility. *Interface Sci.* **2002**, *40*, 99−110.
(36) Morris, P. A.; French, R. H.; Coble, R. L.; Tebbe, F. N.; Chowdhry, U. Clean-Room and CO_2-Laser Processing of Ultra-High-Purity Al_2O_3. *Mater. Res. Soc. Symp. Proc.* **1985**, *60*, 79.
(37) Blendell, J. E.; Bowen, H. K.; Coble, R. L. High Purity Alumina by Controlled Precipitation From Aluminum Sulfate Solutions. *Am. Ceram. Soc. Bull.* **1984**, *63*, 797−802.
(38) Park, C. W.; Yoon, D. Y. Effect of SiO_2, CaO and MgO Additions on The Grain Growth of Alumina. *J. Am. Ceram. Soc.* **2000**, *83*, 2605−2609.
(39) Bae, J.; Baik, S. Abnormal Grain Growth of Alumina. *J. Am. Ceram. Soc.* **1997**, *80*, 1149−1156.
(40) Bae, J.; Baik, S. Determination of Critical Concentrations of Silica and/or Calcia for Abnormal Grain Growth in Alumina. *J. Am. Ceram. Soc.* **1993**, *76*, 1065−1067.
(41) Handwerker, C. A.; Morris, P. A.; Coble, R. L. Effect of Chemical Inhomogeneities on Grain Growth and Microstructure in Al_2O_3. *J. Am. Ceram. Soc.* **1989**, *76*, 130−136.
(42) Bennison, S. J.; Harmer, M. P. Grain-Growth Kinetics for Alumina in The Absence of A Liquid Phase. *J. Am. Ceram. Soc.* **1985**, *68*, C22−C24.
(43) Bennison, S. J.; Harmer, M. P. Effect of MgO Solute on the Kinetics of Grain Growth in Al_2O_3. *J. Am. Ceram. Soc.* **1983**, *66*, C90−C92.
(44) Sakaguchi, I.; Haneda, H.; Srikanth, V.; Ikegami, T. An Effect of Second Phase on Oxygen Grain Boundary Diffusion in MgO-doped Polycrystalline Alumina. *Mater. Res. Bull.* **1996**, *31*, 837−843.
(45) Handwerker, C. A.; Dynys, J. M.; Cannon, R. M.; Coble, R. L. Dihedral Angles in Magnesia and Alumina. *J. Am. Ceram. Soc.* **1990**, *73*, 1371−1377.
(46) Bateman, C. A.; Bennison, S. J.; Harmer, M. P. Mechanism for the Role of Magnesia in the Sintering of Alumina Containing Small Amounts of a Liquid Phase. *J. Am. Ceram. Soc.* **1989**, *72*, 1241−1244.
(47) Berry, K. A.; Harmer, M. P. Effect of MgO Solute on Microstructure Development in Al_2O_3. *J. Am. Ceram. Soc.* **1986**, *69*, 143−149.
(48) Heuer, A. H. The Role of MgO in the Sintering of Alumina. *J. Am. Ceram. Soc.* **1979**, *62*, 317−318.
(49) Johnson, W. C.; Harmer, M. P. A Test of the Second-phase and Impurity-segregation Models for MgO-enhanced Densification of Sintered Alumina. *J. Am. Ceram. Soc.* **1978**, *61*, 110−114.
(50) Coble, R. L. Sintering of Crystalline Solids−II, Experimental Test of Diffusion Models in Porous Compacts. *J. Appl. Phys.* **1961**, *32*, 793−799.
(51) Koo, J. B.; Yoon, D. Y. The Dependence of Normal and Abnormal Grain Growth in Silver on Annealing Temperature and Atmosphere. *Metall. Mater. Trans. A* **2001**, *32*, 469−475.
(52) Lee, S. B.; Hwang, N. M.; Yoon, D. Y.; Henry, M. F. Grain Boundary Faceting and Abnormal Grain Growth in Nickel. *Metall. Mater. Trans. A* **2000**, *31A*, 469−475.
(53) Kaplan, W. D.; Mxillejans, H.; Rühle, M.; Rödel, J.; Claussen, N. Ca Segregation to Basal Surfaces in α-alumina. *J. Am. Ceram. Soc.* **1995**, *78*, 2841−2844.
(54) Swiatnicki, W.; Lartigue-Korinek, S.; Laval, J. Y. Grain Boundary Structure and Intergranular Segregation in Al_2O_3. *Acta Metall. Mater.* **1995**, *43*, 795−805.
(55) Scott, C.; Kaliszewski, M.; Greskovich, C.; Levinson, L. Conversion of Polycrystalline Al_2O_3 Into Single-crystal Sapphire by Abnormal Grain Growth. *J. Am. Ceram. Soc.* **2002**, *85*, 1275−1280.
(56) Kinoshita, M. Boundary Migration of Single Crystal in Polycrystalline Alumina. *Yogyo Kyokaishi* **1974**, *82*, 295−296.
(57) Wei, G. C. Transparent Ceramics for Lighting. *J. Eur. Ceram. Soc.* **2009**, *29*, 237−244.
(58) Kooy, C. In *Science in Ceramic*; Stewart, G. H., Ed.; Academic Press: London, 1962; Vol. *1*, pp 21−34.
(59) Allibert, M. *Slag Atlas*, 2nd ed.; Verlag Stahleisen GmbH: Düsseldorf, 1995.
(60) Li, H.; Yu, G.; Walker, D.; Evans, R. Modelling and Measurement of Polishing Tool Influence Functions for Edge Control. *J. Eur. Opt. Soc.* **2011**, *6*, No. 11048.
(61) Lai, C. C.; Cheng, N. C.; Wang, C. K.; Tjiu, J. W.; Lin, M. Y.; Huang, S. Y. Simple and Efficient Defect-tailored Fiber-based UV-VIS Broadband White Light Generation. *Opt. Express* **2013**, *21*, 14606−14617.